NJC

ROYAL SOCIETY OF CHEMISTRY

PAPER

View Article Online
View Journal | View Issue

Check for updates

Cite this: *New J. Chem.*, 2022, **46**, 9762

Counterion-controlled synthesis of multifunctional iron cobalt mixed oxide laminar superstructures†

Nureena Kanwal,[a] Bilal Akram, *[b] Chaudry Sajed Saraj,[cd] Khalil Ahmad,[a] Shamraiz Hussain Talib[e] and Hafiz Muhammad Asif[f]

Received 29th January 2022,
Accepted 11th April 2022

DOI: 10.1039/d2nj00412g

rsc.li/njc

The design and fabrication of cost-effective multifunctional nanomaterials with well-defined ultrafine nanostructures remains a challenge. Herein, cobalt- and iron-based mixed oxide nanoclusters and laminar superstructures were successfully synthesized through a single step low temperature solution phase route by using good and poor solvent systems. The structure of the as-fabricated material is largely defined by the counterions of the precursor salts. The easily obtained unique FeCo-based mixed oxide nanoclusters and laminar superstructures are not only capable of catalysing the photodegradation of methylene blue (MB) under sunlight, but also behave as outstanding electrocatalysts towards the oxygen evolution reaction (OER). The present findings offer a new insight to rationally design materials with desired structures and functions.

Understanding the structure–activity relationship of nanomaterials is one of the emerging research directions in nanoscience. It has enabled researchers to develop new synthetic strategies and potential applications of various nanostructured materials.[1] When the size of materials approaches to a scale of 1 nm, their physical and chemical features alter significantly.[2] Ultrathin nanomaterials not only feature atomic scale dimensions, but also have unparalleled characteristics in comparison with conventional nanomaterials. Therefore, the controlled and expedient synthesis of ultrafine nanostructures is highly desirable for potential uses in various fields. It has been observed that the growth of the crystals is significantly influenced by the size and surface features of the crystal nuclei. By controlling the size of the crystal nucleus and the solution environment, the crystal can exhibit multi-dimensional growth modes.[3–8] The accumulation of these nano-synthetic technologies has laid a solid foundation for the discovery of new synthetic methodologies and the design of new materials. Amongst different types of nanostructures, laminar superstructures, which possess intermittent multi-level geometry, attract special attention due to higher specific surface area and exceptional stability.[9,10] Although great progress has been made in the field, the synthesis of controlled novel transition metal-based mixed oxides having well-defined laminar micro/nano-architectures is still challenging.

The extensive utilization of transition metal oxides has stimulated an intense interest to understand and tune their features to endow them with new or improved functionalities.[11–13] Iron cobalt (FeCo)-based nanomaterials behave as an important soft magnetic material due to their novel magnetic characteristics, such as large permeability and much higher saturation magnetization. FeCo nanoparticles (NPs) are ideal building units for the construction of nanostructured thin films or bulk magnetic materials.[14,15] Such materials are also equally important for biomedical and energy-related applications.[16,17] However, the poor chemical stability of the NPs limits their large-scale fabrication. Several efforts have been made to synthesize size- and composition-controlled FeCo NPs.[16,18] Desvaux *et al.*[19] reported the fabrication of FeCo NPs through decomposition of organometallic precursors in an inert environment. Another research group reported the fabrication of FeCo and graphite core shell-based nanocomposites through a chemical vapor deposition route and explored their uses in magnetic resonance imaging.[20] There are also a few reports that exist about the fabrication of FeCo-based oxide and layered double hydroxide oxygen evolution electrocatalysts.

---

[a] *Department of Chemistry, Mirpur University of Science and Technology, Mirpur AJ&K, Pakistan*
[b] *Department of Chemistry, Women University of Azad Jammu & Kashmir, Bagh AJ&K, Pakistan. E-mail: bai-l16@tsinghua.org.cn*
[c] *GPL, State Key Lab. of Applied Optics, Changchun Institute of Optics, Fine Mechanics and Physics, Chinese Academy of Sciences, Changchun 130033, China*
[d] *University of Chinese Academy of Sciences, Beijing 100049, China*
[e] *School of Physics, Henan Normal University, Xinxiang 453007, China*
[f] *Institute of Chemical Sciences, Bahauddin Zakariya University Multan, 60800, Punjab, IR, Pakistan*

† Electronic supplementary information (ESI) available. See DOI: https://doi.org/10.1039/d2nj00412g

However, their fabrication often requires higher temperatures and sophisticated synthetic conditions.[21,22] Therefore, a low temperature solution phase route to FeCo mixed oxide-based ultrafine NPs and their assembly into well-defined laminar superstructures is highly desirable for energy and environmental applications but still challenging.

Decided by the intrinsic features of nanomaterials, iron- and cobalt-based mixed oxide nanostructures are generally light sensitive due to their surface plasmon resonance (SPR).[23] Therefore, such materials exhibit high photocatalytic activity. When the size of such materials approaches to a sub-nanometre scale, their surface will be enriched with more electrons and active centres that can further enhance their catalytic performance. Considering the possible existence of synergistic effects, the nanocomposite of iron and cobalt mixed oxides is anticipated to possess more outstanding features in catalytic, optical and energy-related fields.

Herein we report the successful fabrication of multifunctional ultrafine FeCo mixed oxide nanoclusters and self-assembled laminar superstructures using a low temperature solution phase route. Our newly designed mixed oxide materials are multifunctional in nature as evidenced by their outstanding performance towards the electrocatalytic oxygen evolution reaction and photocatalytic dye degradation.

A Good and poor solvent system-based low temperature solution phase synthetic route was developed to obtain FeCo mixed oxide ultrafine nanoparticles (FCNPs) and laminar superstructures (FCLSs). Fig. 1a reveals the schematic of formation of the FCNPs and FCLSs. The structural analysis of the synthesized test analytes was accomplished *via* transmission electron microscopy (TEM). Fig. 1b and d show the TEM images of the products synthesized using different precursor salts. The product obtained using acetate precursor salts of iron and cobalt has well-defined nanocluster like structure FCNPs (Fig. 1b). The size of the nanoparticles was distributed uniformly throughout with a mean diameter of around 2 nm as indicated by Fig. 1c. The product obtained with sulphate precursors has a unique well-defined laminar superstructure (Fig. 1d). These laminar superstructures seem to be developed from ultrafine nanoparticles (Fig. S1, ESI†). FCLSs have been obtained by carefully controlling the anisotropic growth kinetics through the low-temperature decomposition of the metal precursors and the use of a moderately reducing environment. ODA was used as a surfactant as well as a reducing agent. The precursor salt is decomposed followed by nucleation and growth to well-developed NPs. The higher surface energy of the obtained NPs is the driving force behind the self-assembly to laminar superstructures. The mechanistic details of the formation of mixed oxides are given in the ESI† in Scheme S1. The above results indicate that the counterions of the precursor salts have a substantial influence on the determination of the structures of the final product. The sulphate ions behave as assembling agents. The effect of counterions on the morphology was further evidenced by conducting the same experiment using chloride precursors of both metals. Fig. S2 (ESI†) indicates the formation of the product from chloride precursors of both metals. Ultrathin nanosheets were obtained in this case. The obtained nanosheets are free floating in solution, which get aggregated during analyte preparation. The high-resolution TEM image in Fig. S2 (ESI†) confirms the ultrathin nature and stacking behaviour of the synthesized individual nanosheets. In each case, the formation of a well-defined nanostructure indicates the effectiveness of our developed synthetic strategy.

The compositional analysis of the synthesized nanostructures has been done using XRD. The XRD patterns shown in Fig. 2a reveal that both the FCNPs and FCLSs have a similar pattern. Both the products do not have sharp peaks, indicating their poor crystallinity. However, there are a few weak peaks that can be indexed well with $CoFe_2O_4$ (PDF#22-1086). A few weak peaks around 2 theta values of 18, 30 and 35 degrees refer to (111), (220) and (311) faces of cobalt iron oxide $CoFe_2O_4$. FTIR spectra of both samples show two clearly expressed bands in the 700–500 cm^{-1} region. The literature reported value for cobalt oxide is 580 cm^{-1}. Bonding of Co with Fe causes shifting of the bands towards lower wavenumbers. FeCo mixed oxide

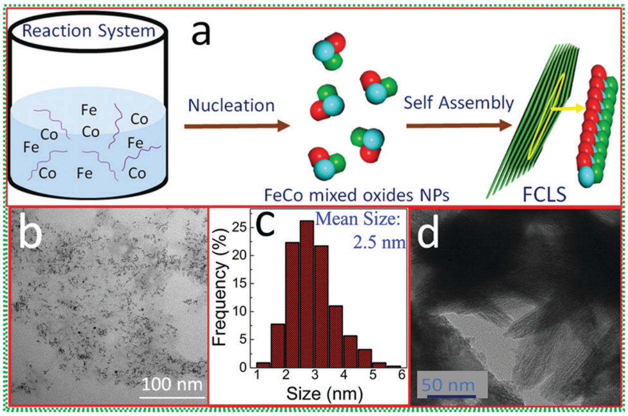

Fig. 1 (a) Schematic of the formation of FeCo mixed oxide laminar superstructures (FCLSs), (b) TEM image, and (c) particle size distribution of FeCo mixed oxide nanoclusters (FCNPs) and (d) TEM image of FCLSs.

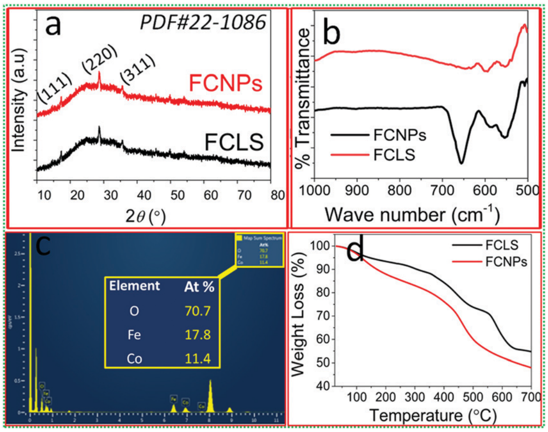

Element	At %
O	70.7
Fe	17.8
Co	11.4

Fig. 2 (a) XRD patterns, (b) FTIR spectra, and (d) TGA of both FCLSs and FCNPs and (c) EDX of representative FCLSs.

stretching can be clearly observed at 553 cm^{-1} to 642 cm^{-1}. Bonding of two metals causes shifting of the bands towards lower wavenumbers (Fig. 2b). In FTIR, shifting of the bands towards lower wave numbers confirmed the formation of mixed oxides.[24] The structural composition was further confirmed by using energy dispersive spectroscopy (EDX) by taking the synthesized FCLSs as a representative of the materials. The EDX spectrum of the laminar superstructures is shown in Fig. 2c. The spectrum shows that the synthesized FCLSs are well composed of both iron and cobalt.

The thermal stability of the FCLSs and FCNPs was investigated through TGA (Fig. 2d), and both samples reveal significant weight loss that may be attributed to the removal of solvents and surface bound organic ligands. There is almost 8–10% weight loss up to 250 °C temperature, which refers to the presence of ethanol/hexane solvents and physically adsorbed water. Almost 16–18% weight loss was observed in the 250–500 °C temperature range, which was attributed to the removal of chemically bound water and organics. Our solvent system is composed of long carbon chain organic ligands that are ODA and OA, and hence contributed significantly to the total weight content of our product. The remaining 20% weight loss was attributed to the removal of carbon contents. However, there is relatively less weight loss in the case of FCLSs than FCNPs, which indicates the better stability of the FCLSs.

The valence state and electronic environment of various components of the FCLSs were analyzed using X-ray photoelectron spectroscopy (XPS). Fig. 3a–c represent the high-resolution spectra of characteristic elements present in the FCLSs. There is the appearance of a single peak at a binding energy (BE) of 529.7 eV in the spectrum of O 1s, which refers to the O^{2-} state forming oxide. The BEs of Fe 2p3/2 and 2p1/2 were observed at 710.6 and 723.5 eV, respectively, which confirms the +3 oxidation state of iron. Similarly, Co exhibits its 2p3/2 peak at 779.7 and 2p1/2 peak at 795.3 referring to the +2 oxidation state. As evidenced from the XPS observation, both the Co and Fe are in oxide forms rather than in metallic forms.

The optical properties of the prepared samples were investigated using diffused reflectance spectroscopy. Both the FCLSs and FCNPs show broad absorption bands in the wavelength window ranging from 300 nm to 600 nm. The darker colour and ultrafine nature of the product also evidenced the broad range absorption (Fig. S3, ESI†). As the size of the product decreases to the sub-manometer scale, the electronic levels increase and the band gap decreases, which leads to the absorption in the visible region (red shift). Taking advantages of the broad range absorption, the newly designed FCLSs and FCNPs were potentially employed as excellent photocatalysts for the degradation of methylene blue (MB) as a model pollutant.

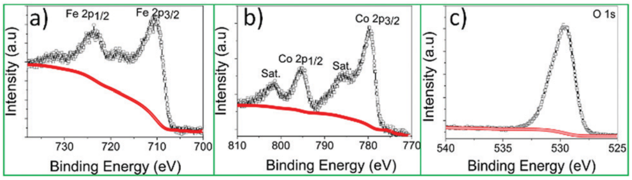

Fig. 3 XPS spectra of (a) Fe, (b) Co and (c) O of FCLSs.

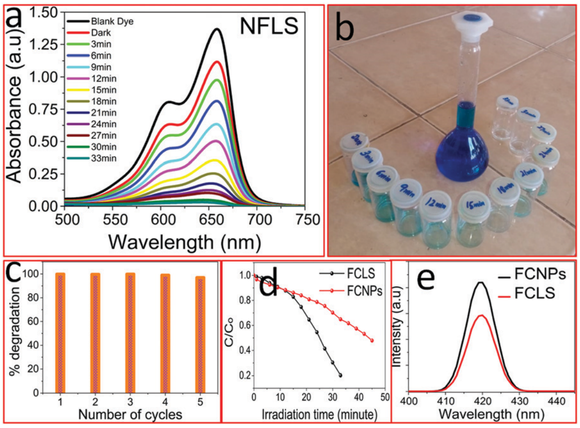

Fig. 4 (a) Time-dependent UV/vis absorption spectra of MB dye solution. (b) Photographs showing a gradual change in colour. (c) Reusability of the FCLS photocatalyst for oxidative photodegradation of MB. (d) Comparative degradation efficiencies of FCLSs and FCNPs. (e) PL spectra of FCLSs and FCNPs.

The photocatalytic performance of the prepared samples was analysed by taking MB as a model pollutant. MB is a very common hazardous textile dye and therefore its degradation remains a subject of interest from the last few decades.[25] Fig. 4a and b reveal the periodic photocatalytic oxidative degradation of MB using FCLSs as a catalyst. The catalyst manifests excellent performance towards MB degradation. The catalyst's stability was investigated by repeatedly using the same catalyst. The catalyst was recovered by centrifugation. The catalyst exhibits the best stability as evidenced by the same performance for five duplicate operations (Fig. 4c). In order to investigate the structure–activity relationship, the oxidative phtodegradation was also investigated using FCNPs as a catalyst (Fig. S4, ESI†). The FCLSs exhibit superior performance compared to the FCNPs as indicated in Fig. 4d. Under light irradiation in a short period of 30 min, the FCLSs are capable of degrading over 99% of the dye, while the FCNPs degrade only 80% of the dye in the same period of 30 minutes as shown in Fig. S5 (ESI†). The superior performance of the FCLSs than the FCNPs can be explained on the basis of the structure. In the case of FCLSs, the self-assembly leads to a structure where the possibility of electron–hole recombination is minimum, hence a better photodegradaion efficiency. This can be evidenced through the photoluminescence (PL) spectrum shown in Fig. 4e. Both samples of the same concentration manifest different peak intensities at the same wavelength. The peak referring to FCLSs is less intense indicating that it has minimum charge recombination and maximum free electrons, which endows the material with the best photocatalytic behaviour. Moreover the higher BET surface area (Fig. S6, ESI†) of the FCLSs (137.63 $m^2\ g^{-1}$) as compared to the FCNPs (79.72 $m^2\ g^{-1}$) further evidenced the superior photocatalytic performance of the FCLSs.

Control experiments reveal that no significant dye degradation was observed with individual FCLSs (Fig. S7, ESI†) or oxidant, *i.e.*, H_2O_2 (Fig. S8, ESI†). However the observed performance of the individual FCLSs and H_2O_2 reveals that both have potential for activation by solar light irradiation. This individual FCLS performance can be attributed to the augmentation in the available active sites required for the formation of a large number of hydroxyl radicals (reactive oxygen species) in the reaction medium, which are responsible for the degradation and mineralization of the MB dye. Similarly, the photolysis of H_2O_2 can also lead to hydroxyl radicals responsible for degradation. The degradation efficiency improved remarkably with both FCLS and H_2O_2. This enhancement in the performance may be due to the interaction effect of the two species *i.e.*, photocatalyst and H_2O_2. H_2O_2 is thought to have two important functions in the presence of the FCLS photocatalyst, hindering the recombination of electrons and holes *via* reaction between H_2O_2 and the electrons and improving the generation of hydroxyl radicals as indicated in the following equation:

$$\text{Photocatalyst} \xrightarrow{h\nu} \text{Photocatalyst} + \text{e}^- + \text{h}^+$$

$$\text{e}^- + H_2O_2 \rightarrow \text{HO}^\circ + \text{OH}^-$$

The as fabricated FCLSs and FCNPs were further screened for the electrocatalytic OER in a basic (1.0 M KOH) medium. Fig. 5(a) shows iR-corrected linear sweep voltammetry (LSV) curves for FCNP, FCLS and CC electrodes along with an IrO_2 electrode for reference. Briefly, the FCLSs show a lower overpotential of 330 mV at a current density of 10 mA cm^{-2} than that of the FCNPs (378 mV), which is comparable to that of the state-of-the-art IrO_2 (291 mV) OER catalyst. It is clear from these curves that the FCLSs are a better OER electrocatalyst with a higher current density. For instance, at an overpotential of 450 mV in Fig. 5(a), the FCLS catalyst possesses a current density of ~175 mA cm^{-2}, which is about 3 times higher than that of the FCNP (~60 mA cm^{-2}) catalyst. Similarly, the η_{100} (412 mV) overpotential value for the FCLS sample is higher than those of the FCNP and IrO_2 samples (Table S1, ESI†). The OER kinetics of the catalysts are also probed by Tafel plots; the Tafel slopes of the as-synthesized catalysts were calculated from the corresponding polarization curves presented in Fig. 5(b), and the estimated Tafel slopes (η *vs.* $\log I$) for the catalysts CC, FCNPs, and FCLSs are ~70, 47, and 45 mV dec^{-1}. The Tafel slopes and different overpotential values for all the as-synthesized catalysts are summarized as Table S1 in the ESI.† It is an established fact that a smaller value of Tafel slope indicates swift reaction kinetics for the OER and high catalytic activity.[26]

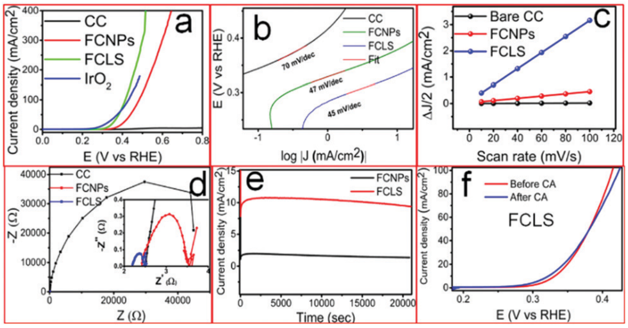

Fig. 5 OER performance of FCLSs and FCNPs: (a) Polarization curves, (b) corresponding Tafel slopes, (c) corresponding Cdl, (d) corresponding Nyquist plots, (e) corresponding chronoamperometry (CA) tests and (f) LSV curves of the FCLSs before and after CA.

Mostly, the electrochemically active surface area (ECSA) and the conductivity are the key factors affecting the catalytic activity. The improved OER performance of the as-fabricated test analytes is further evidenced by estimating the ECSA. The ECSA is estimated by using the corresponding double-layer capacitance (C_{dl}) value extracted from the cyclic voltammetry (CV) curves recorded in the non-faradaic region at different scan rates (Fig. 5c and Fig. S9, ESI†). The ECSA of the catalysts was calculated from the double-layer capacitance value by using the equation:[27]

$$\text{ECSA} = \frac{C_{\text{dl,catalysts}}}{C_{\text{dl,CC}}} \tag{1}$$

where $C_{\text{dl,catalysts}}$ is the double-layer capacitance of the as-synthesized catalysts and $C_{\text{dl,CC}}$ is the double-layer capacitance of bare carbon cloth. The FCLSs exhibit the largest C_{dl} value (30.6 mF cm^{-2}) as compared to the FCNPs (4.2 mF cm^{-2}), indicating a larger ECSA value for the FCLSs (~153 cm^2), which is about 7.2 times that of the FCNPs. (See ESI† Table S3).

Moreover, to gain further insight into the electrode kinetics, the electrochemical impedance spectroscopy (EIS) of the catalysts was performed, the Nyquist plots are presented in Fig. 5d. The charge-transfer resistance (R_{ct}) is estimated from the Nyquist plots, where R_{ct} is the diameter of the semi-circle. The test analyte FCLSs (2.49 Ω) have substantially lower charge-transfer resistance than the FCNPs (3.48 Ω), and CC (43.9 kΩ) sample, resulting in a comparatively efficient charge transfer at the electrode-adsorbate interface for the oxidation of intermediates (OH*, OOH*, and O*), adsorbed on the electrocatalyst surface, responsible for the OER.[28]

The OER long-term durability of both samples was investigated through choronoammperometery (CA) tests at a fixed anodic overpotential of 330 mV. Thus, the current density remains constant for 20 000s of electrolysis (95.5% of the initial value). Fig. 5(e) reveals the excellent stability of the FCLS catalyst during the OER. However, the current density of the FCNP catalyst is only 72.2% of its initial value under similar conditions. Furthermore, the LSV curves recorded before and after the durability test in Fig. 5(f) are almost unchanged, which further indicates the excellent stability of the FCLS catalyst. These findings evidenced the outstanding long-term stability of the FCLS catalyst during electrocatalysis.

Our newly designed FeCo mixed oxide-based laminar superstructures show excellent performance towards the OER and are comparable, or even superior to most of the already reported FeCo-based electrocatalysts, as summarized in Table S4 (ESI†). The superior performance was credited to the unique self-assembled laminar superstructures.

In summary, we have successfully fabricated well-defined FeCo mixed oxide laminar superstructures, as an efficient photocatalyst and electrocatalyst, through a single-step low temperature solution phase route. The results demonstrated that the counterions of the precursor salts play a significant role in the determination of the structure of the final product. The self-assembled laminar structure of FCLSs is the determining factor to boost the OER and photocatalytic activity. Such a synthetic approach may provide a valuable insight into the rational design of multi-component self-assembled superstructures with potential applications in renewable energy and environmental remediation.

Conflicts of interest

The authors declare no competing financial interest.

Notes and references

1 Y. Yang, Y. Yang, S. Chen, Q. Lu, L. Song, Y. Wei and X. Wang, *Nat. Commun.*, 2017, **8**, 1–9.
2 S. Hu and X. Wang, *Chem. Soc. Rev.*, 2013, **42**, 5577–5594.
3 F. Song and X. Hu, *Nat. Commun.*, 2014, **5**, 1–9.
4 W. Ma, R. Ma, C. Wang, J. Liang, X. Liu, K. Zhou and T. Sasaki, *ACS Nano*, 2015, **9**, 1977–1984.
5 C. Andronescu, S. Barwe, E. Ventosa, J. Masa, E. Vasile, B. Konkena, S. Möller and W. Schuhmann, *Angew. Chem., Int. Ed.*, 2017, **56**, 11258–11262.
6 B. Akram, W. Shi, H. Zhang, S. Ullah, M. Khurram and X. Wang, *Angew. Chem.*, 2020, **132**, 8575–8579.
7 B. Akram, Q. Lu and X. Wang, *ACS Mater. Lett.*, 2020, **2**, 461–465.
8 B. Akram and X. Wang, *Langmuir*, 2019, **35**, 10246–10266.
9 C. Gu, X. Ge, X. Wang and J. Tu, *J. Mater. Chem. A*, 2015, **3**, 14228–14238.
10 H. Zhang, H. Li, B. Akram and X. Wang, *Nano Res.*, 2019, **12**, 1327–1331.
11 C. Yuan, H. B. Wu, Y. Xie and X. W. Lou, *Angew. Chem., Int. Ed.*, 2014, **53**, 1488–1504.
12 F. Wu, J. Bai, J. Feng and S. Xiong, *Nanoscale*, 2015, **7**, 17211–17230.
13 M. Ahmad, M. A. Khan, A. Mahmood, S.-S. Liu, A. H. Chughtai, W.-C. Cheong, B. Akram and G. Nasar, *Ceram. Int.*, 2018, **44**, 5433–5439.
14 H. Zeng, J. Li, J. P. Liu, Z. L. Wang and S. Sun, *Nature*, 2002, **420**, 395–398.
15 H. Zeng, J. Li, Z. Wang, J. Liu and S. Sun, *Nano Lett.*, 2004, **4**, 187–190.
16 G. S. Chaubey, C. Barcena, N. Poudyal, C. Rong, J. Gao, S. Sun and J. P. Liu, *J. Am. Chem. Soc.*, 2007, **129**, 7214–7215.
17 S. Behrens, H. Bönnemann, N. Matoussevitch, A. Gorschinski, E. Dinjus, W. Habicht, J. Bolle, S. Zinoveva, N. Palina and J. Hormes, *J. Phys.: Condens. Matter*, 2006, **18**, S2543.
18 G. Viau, F. Fievet-Vincent and F. Fievet, *J. Mater. Chem.*, 1996, **6**, 1047–1053.
19 C. Desvaux, C. Amiens, P. Fejes, P. Renaud, M. Respaud, P. Lecante, E. Snoeck and B. Chaudret, *Nat. Mater.*, 2005, **4**, 750–753.
20 W. S. Seo, J. H. Lee, X. Sun, Y. Suzuki, D. Mann, Z. Liu, M. Terashima, P. C. Yang, M. V. Mcconnell and D. G. Nishimura, *Nat. Mater.*, 2006, **5**, 971–976.
21 C. C. McCrory, S. Jung, J. C. Peters and T. F. Jaramillo, *J. Am. Chem. Soc.*, 2013, **135**, 16977–16987.
22 C. Xiao, X. Lu and C. Zhao, *Chem. Commun.*, 2014, **50**, 10122–10125.
23 K. Lee, W. S. Seo and J. T. Park, *J. Am. Chem. Soc.*, 2003, **125**, 3408–3409.
24 S. G. Christoskova, M. Stoyanova and M. Georgieva, *Appl. Catal., A*, 2001, **208**, 235–242.
25 B. Akram, K. Ahmad, J. Khan, B. A. Khan and J. Akhtar, *New J. Chem.*, 2018, **42**, 10947–10952.
26 X. Han, C. Yu, S. Zhou, C. Zhao, H. Huang, J. Yang, Z. Liu, J. Zhao and J. Qiu, *Adv. Energy Mater.*, 2017, **7**, 1602148.
27 X. Luo, P. Ji, P. Wang, R. Cheng, D. Chen, C. Lin, J. Zhang, J. He, Z. Shi and N. Li, *Adv. Energy Mater.*, 2020, **10**, 1903891.
28 C. S. Saraj, S. C. Singh, A. Shukla, W. Yu, M. U. Fayyaz and C. Guo, *ChemElectroChem*, 2021, 209–217.